Vacuum electromagnetic counterparts of binary black-hole mergers

Philipp Mösta,[1] Carlos Palenzuela,[2,1] Luciano Rezzolla,[1] Luis Lehner,[3,4,5] Shin'ichirou Yoshida,[6,1] and Denis Pollney[1]

[1]*Max-Planck-Institut für Gravitationsphysik, Albert-Einstein-Institut, Potsdam-Golm, Germany*
[2]*Canadian Institute of Theoretical Astrophysics, Toronto, Ontario, Canada*
[3]*Perimeter Institute for Theoretical Physics, Waterloo, Ontario, Canada*
[4]*Department of Physics, University of Guelph, Guelph, Ontario, Canada*
[5]*Canadian Institute for Advanced Research, Cosmology & Gravity Program*
[6]*Department of Earth Science and Astronomy, Graduate School of Arts and Sciences, University of Tokyo*

As one step towards a systematic modeling of the electromagnetic (EM) emission from an inspiralling black hole binary we consider a simple scenario in which the binary moves in a uniform magnetic field anchored to a distant circumbinary disc. We study this system by solving the Einstein-Maxwell equations in which the EM fields are chosen with strengths consistent with the values expected astrophysically and treated as test fields. Our initial data consists of a series of binaries with spins aligned or antialigned with the orbital angular momentum and we study the dependence of gravitational and EM signals with different spin configurations. Overall we find that the EM radiation in the lowest $\ell = 2$, $m = 2$ multipole accurately reflects the gravitational one, with identical phase evolutions and amplitudes that differ only by a scaling factor. This is no longer true when considering higher ℓ modes, for which the amplitude evolution of the scaled EM emission is slightly larger, while the phase evolutions continue to agree. We also compute the efficiency of the energy emission in EM waves and find that it scales quadratically with the total spin and is given by $E_{\rm EM}^{\rm rad}/M \simeq 10^{-15}(M/10^8 M_\odot)^2(B/10^4{\rm G})^2$, hence 13 orders of magnitude smaller than the gravitational energy for realistic magnetic fields. Although large in absolute terms, the corresponding luminosity is much smaller than the accretion luminosity if the system is accreting at near the Eddington rate. Most importantly, this EM emission is at frequencies of $\sim 10^{-4}(10^8 M_\odot/M)$ Hz, which are well outside those accessible to astronomical radio observations. As a result, it is unlikely that the EM emission discussed here can be detected *directly* and simultaneously with the gravitational-wave one. However, indirect processes, driven by changes in the EM fields behavior could yield observable events. In particular we argue that if the accretion rate of the circumbinary disc is small and sufficiently stable over the timescale of the final inspiral, then the EM emission may be observable *indirectly* as it will alter the accretion rate through the magnetic torques exerted by the distorted magnetic field lines.

I. INTRODUCTION

Gravitational-wave (GW) astronomy promises to revolutionize our understanding of a number of astrophysical systems. Several Earth-based detectors (LIGO, Virgo, GEO) are already operating at their designed sensitivities and will be further upgraded in the coming years. Additionally, space-borne detectors are being considered and might become a reality in the coming decade. The ability to harness the information carried by GWs will soon provide a completely new way to observe the universe around us. These detectors, along with increasingly sensitive electromagnetic (EM) telescopes, will provide insights likely to affect profoundly our understanding of fundamental physics and the cosmos (see e.g. [1,2] for a recent and detailed discussions of the astrophysics and cosmology that will be possible with the detection of GWs)

Among the most promising sources of detectable GWs are systems composed of binary black holes which, as they come together and merge, radiate copious amounts of energy in the form of gravitational radiation. When these black holes are supermassive, with masses $M \gtrsim 10^6 M_\odot$, the cosmological and astrophysical conditions leading to their formation will be such that prior to the merger they will be surrounded by a gas or plasma that could also radiate electromagnetically. Indeed, within the context of galaxy mergers, such a scenario will typically arise as the central black hole in each of the colliding galaxies sinks towards the gravitational center, eventually forming a binary. In such a process, the binary will generically find itself inside a circumbinary disc which might be a catalyst of observable emissions as it interacts with the black holes [3–5]. Within this context, several possibilities are actively being investigated. Among these, several studies have (with varying degrees of approximations) concentrated on understanding emissions by the disc due to the interaction with a recoiling, or a mass-reduced final black hole [6–11] and remnant gas around the black holes [12–15].

A further intriguing possibility for such interaction is through EM fields and, in particular, through the gravitomagnetic deformation of magnetic fields, anchored to the disc, around the central region where the black holes

inspiral and merge. As the black holes proceed in an ever shrinking orbit towards their ultimate coalescence, they will twist and stir the EM fields and thus affect their topology. Moreover, the spacetime dynamics might impact the fields in such a strong way as to generate EM energy fluxes which may reach and impact the disc and affect possible gas in the black holes' vicinity. Last, but certainly not least, as the merger takes place the system could acquire (at least at much later times) a configuration where emissions through the Blandford-Znajek mechanism may take place [16].

The initial step towards understanding this system was taken in [17,18] and highlighted the possible phenomenology in the system. Although this first investigation was restricted to the simplest case of an equal-mass, nonspinning binary, it provided a proof of principle examination of possible EM counterparts resulting from binary mergers. The work presented here extends the study carried out in [17,18] on several fronts. First, it considers an broader class of binaries, with and without net spins which are aligned or counter-aligned with the orbital angular momenta (in the case of supermassive black holes, these configurations are indeed the most likely to be produced [19,20]). Second, it studies binaries from larger separations, thus allowing for a clearer modeling of the inspiral. Third, it examines more closely the energy emissions in both channels and compares the total output's dependence on final black-hole spin. Finally, it assesses the direct detectability of the EM radiation produced, and considers the astrophysical impact it may have on the surrounding accretion disc. In addition, while sharing the same astrophysical scenario, the methodological approach adopted here also differs from that of [17,18] in at least three important ways. First, we here explicitly impose the test-field limit by setting to zero the stress-energy tensor on the right-hand side of the Einstein equations. Second, we employ a different formulation of Einstein equations, i.e., a conformal transverse-traceless one in place of a generalized-harmonic one. Third, we use a distinct computational infrastructure based on CACTUS and CARPET rather than the HAD code which was instead used in [17,18]). The excellent agreement in the phenomenology observed, in cases considered in both works, gives a strong further indication of the correctness of the results obtained.

Our analysis shows that the EM-wave emission in the lowest $\ell = 2$, $m = 2$ multipole reflects in a spectacular way the gravitational one and that the phase and amplitude evolution differ only by a scaling factor. This is no longer true when considering higher ℓ modes, for which the amplitude evolution of the EM emission is slightly larger. We also find that the efficiency of the energy emission in EM waves scales quadratically with the total spin and is given, for realistic magnetic fields, by $E_{\rm EM}^{\rm rad}/M \simeq 10^{-15}(M/10^8 M_\odot)^2 (B/10^4 \ {\rm G})^2$. For expected fields of 10^4 G this energy loss is 13 orders of magnitude smaller than the gravitational one. In addition, the corresponding EM luminosity is much smaller than that of accretion, if the system is accreting at near the Eddington rate. Most importantly, this emission is at frequencies of $\sim 10^{-4}(10^8 M_\odot/M)$ Hz, which lies outside the range of astronomical radio observations. As a result, it is highly unlikely that the EM emission discussed here can be detected directly and simultaneously with the GW one. Other processes however could be affected by this flux of EM energy and produce detectable effects. For instance, if the accretion rate of the circumbinary disc is small and sufficiently stable over the timescale of the final inspiral, then the EM emission may be, in particular, observable indirectly as it will alter the accretion rate through the magnetic torques exerted by the distorted magnetic-field lines.

This work is organized as follows: Sec. II presents an overview of both Maxwell and Einstein equations as implemented within the formulation of the Einstein equations. The physical and astrophysical setup adopted in our simulations is discussed in Sec. III, while Sec. IV is dedicated to the analysis of the EM fields for isolated black holes, either nonspinning or with spin aligned with the orbital angular momentum. Sec. V collects instead our results for the different binaries considered, while the assessment of the astrophysical impact of the EM emission is presented in Sec. VI. We conclude in Sec. VII with final comments and discussions.

II. THE EVOLUTION EQUATIONS

We solve the Einstein-Maxwell system to model the interaction of an inspiraling black-hole binary with an externally sourced magnetic field in an electro-vacuum spacetime. More specifically, we solve the Einstein equations

$$R_{\mu\nu} - \tfrac{1}{2}R g_{\mu\nu} = 8\pi T_{\mu\nu}, \tag{1}$$

where $g_{\mu\nu}$, $R_{\mu\nu}$, and $T_{\mu\nu}$ are the metric, the Ricci and the stress-energy tensor, respectively, together with an extension of Maxwell equations in absence of currents [21,22],

$$\nabla_\mu(F^{\mu\nu} + g^{\mu\nu}\Psi) = -\kappa t^\nu \Psi, \tag{2}$$

$$\nabla_\mu(^*F^{\mu\nu} + g^{\mu\nu}\phi) = -\kappa t^\nu \phi \tag{3}$$

when written as conservation laws for the Faraday tensor $F_{\mu\nu}$ and of its dual $^*F_{\mu\nu}$. Note that we have here introduced two extra scalar fields Ψ and ϕ, which are initially zero and whose evolution drives the system to a satisfaction of the EM constraints (see discussion below). The two systems are coupled through the stress-energy tensor,

$$T_{\mu\nu} = \frac{1}{4\pi}\left[F_\mu{}^\lambda F_{\nu\lambda} - \frac{1}{2}g_{\mu\nu}F^{\lambda\sigma}F_{\lambda\sigma}\right]. \tag{4}$$

Note also that since our stress-energy tensor is not identically zero, the binary is not in vacuum, at least within a

strict general-relativistic sense. However, because the sources of the EM fields are not part of our description and we simply consider EM fields, our setup will be that of an "electromagnetic-vacuum," which we will simply refer to as "vacuum."

A. The Einstein equations

The numerical solution of the Einstein equations has been performed using a three-dimensional finite-differencing code solving a conformal-traceless "3 + 1" formulation of the Einstein equations (see [23] for the full expressions in vacuum and [24] for spacetimes with matter) using the CACTUS Computational Toolkit [25] and the CARPET [26] adaptive mesh-refinement driver. Recent developments, such as the use of 8th-order, finite-difference operators or the adoption of a multiblock structure to extend the size of the wave zone have been recently presented in [23,27]. Here, however, to limit the computational costs and because a very high accuracy in the waveforms is not needed, the multiblock structure was not used. For compactness we will not report here the details of the formulation of the Einstein equations solved or the form of the gauge conditions adopted. All of these aspects are discussed in detail in [23], to which we refer the interested reader.

B. The Maxwell equations

Maxwell Eqs. (2) and (3) take a more familiar form when represented in terms of the standard electric and magnetic fields. These are defined by the following decomposition of the Faraday tensor:

$$F^{\mu\nu} = t^\mu E^\nu - t^\nu E^\mu + \epsilon^{\mu\nu\alpha\beta}B_\alpha t_\beta, \qquad (5)$$

$$^*F^{\mu\nu} = t^\mu B^\nu - t^\nu B^\mu - \epsilon^{\mu\nu\alpha\beta}E_\alpha t_\beta; \qquad (6)$$

where t^μ is the unit time vector associated with a generic normal observer to the hypersurfaces. The vectors E^μ and B^μ are the (purely spatial, $E^\mu t_\mu = B^\mu t_\mu = 0$) electric and magnetic fields measured by such observer.

As mentioned above, we adopt an extended version of Maxwell's equations which introduces two extra scalar fields Ψ and Φ. This extension induces evolution equations for the EM constraints ($\nabla_i E^i = 0 = \nabla_i B^i$) described by damped wave equations and so control dynamically these constraints. In terms of E^μ and B^μ the 3 + 1 version of (2) and (3) results,

$$\mathcal{D}_t E^i - \epsilon^{ijk}\nabla_j(\alpha B_c) + \alpha\gamma^{ij}\nabla_j\Psi = \alpha K E^i, \qquad (7)$$

$$\mathcal{D}_t B^i + \epsilon^{ijk}\nabla_j(\alpha E_c) + \alpha\gamma^{ij}\nabla_j\Phi = \alpha K B^i, \qquad (8)$$

$$\mathcal{D}_t \Psi + \alpha\nabla_i E^i = -\alpha\kappa\Psi, \qquad (9)$$

$$\mathcal{D}_t \Phi + \alpha\nabla_i B^i = -\alpha\kappa\Phi. \qquad (10)$$

where $\mathcal{D}_t \equiv (\partial_t - \mathcal{L}_\beta)$ and $\mathcal{L}_\beta$ is the Lie derivative along

the shift vector β. Exploiting that the covariant derivative in the second term of (8) and (9) reduces to a partial one

$$\epsilon^{ijk}\nabla_j B_k = \epsilon^{ijk}(\partial_j + \Gamma^c_{kj}B_k) = \epsilon^{ijk}\partial_j B_k, \qquad (11)$$

and using a standard conformal decomposition of the spatial three-metric

$$\tilde{\gamma}_{ij} = e^{4\phi}\gamma_{ij}; \qquad \phi = \frac{1}{12}\ln\gamma \qquad (12)$$

one obtains the final expressions

$$\mathcal{D}_t E^i - \epsilon^{ijk}e^{4\phi}[(\partial_j\alpha)\tilde{\gamma}_{ck}B^c + \alpha(4\tilde{\gamma}_{ck}\partial_j\phi + \partial_j\tilde{\gamma}_{ck})B^c$$
$$+ \alpha\tilde{\gamma}_{ck}\partial_j B^c] + \alpha e^{-4\phi}\tilde{\gamma}^{ij}\nabla_j\Psi = \alpha K E^i, \qquad (13)$$

$$\mathcal{D}_t B^i + \epsilon^{ijk}e^{4\phi}[(\partial_j\alpha)\tilde{\gamma}_{ck}E^c + \alpha(4\tilde{\gamma}_{ck}\partial_j\phi + \partial_j\tilde{\gamma}_{ck})E^c$$
$$+ \alpha\tilde{\gamma}_{ck}\partial_j E^c] + \alpha e^{-4\phi}\tilde{\gamma}^{ij}\nabla_j\Phi = \alpha K B^i, \qquad (14)$$

$$\mathcal{D}_t \Psi + \alpha\nabla_i E^i = -\alpha\kappa\Psi, \qquad (15)$$

$$\mathcal{D}_t \Phi + \alpha\nabla_i B^i = -\alpha\kappa\Phi. \qquad (16)$$

Notice that the standard Maxwell equations in a curved background are recovered for $\Psi = \Phi = 0$. The Ψ and Φ scalars can then be considered as the normal-time integrals of the standard divergence constraints

$$\nabla_i E^i = 0, \qquad \nabla_i B^i = 0. \qquad (17)$$

These constraints propagate with light speed and are damped during the evolution.

As mentioned above, the coupling between the Einstein and Maxwell equations takes place via the inclusion of a nonzero stress-energy tensor (cf. the set of equations presented in [24]) for the EM fields and which is built in terms of the Faraday tensor as described in (4). More specifically, the relevant components of the stress-energy tensor can be obtained in terms of the electric and magnetic fields, that is

$$\tau = \frac{1}{8\pi}(E^2 + B^2), \qquad S_i = \frac{1}{4\pi}\epsilon_{ijk}E^j B^k, \qquad (18)$$

$$S_{ij} = \frac{1}{4\pi}\left[-E_i E_j - B_i B_j + \frac{1}{2}\gamma_{ij}(E^2 + B^2)\right] \qquad (19)$$

where $E^2 \equiv E^k E_k$ and $B^2 \equiv B^k B_k$. The scalar component τ can be identified with the energy density of the EM field (i.e., ρ_{ADM} in [24]) and the energy flux S_i is the Poynting vector. As already discussed in the Introduction, we stress again that the EM energies considered here are so small when compared with the gravitational ones that the contributions of the stress-energy tensor to the right-hand side of the Einstein Eq. (1) are comparatively negligible and thus effectively set to zero[1]

---

[1]The fully coupled set of the Einstein-Maxwell equations was considered in [17,18] and the comparison with the results obtained here suggests that for the fields below 10^8 G, the use of the test-field approximation is justified.

C. Analysis of radiated quantities

The calculation of the EM and gravitational radiation generated during the inspiral, merger, and ringdown is arguably the most important aspect of this work as it allows us to establish on a firm basis whether a clear correlation should be expected between the two forms of radiation. We compute the gravitational radiation via the Newman-Penrose curvature scalar Ψ_4 defined as

$$\Psi_4 \equiv -C_{\alpha\beta\gamma\delta} n^\alpha \bar{m}^\beta n^\gamma \bar{m}^\delta, \qquad (20)$$

where $C_{\alpha\beta\gamma\delta}$ is the Weyl curvature tensor, which is projected onto a null frame, $\{l, n, m, \bar{m}\}$. In practice, we define an orthonormal basis in the three space $(\hat{r}, \hat{\theta}, \hat{\phi})$, centered on the Cartesian grid center and oriented with poles along $\hat{z}$. The normal to the slice defines a timelike vector $\hat{t}$, from which we construct the null frame

$$l = \frac{1}{\sqrt{2}}(\hat{t} - \hat{r}), \qquad n = \frac{1}{\sqrt{2}}(\hat{t} + \hat{r}), \qquad m = \frac{1}{\sqrt{2}}(\hat{\theta} - \mathrm{i}\hat{\phi}). \qquad (21)$$

We then calculate Ψ_4 via a reformulation of (20) in terms of Arnowitt-Deser-Misner (ADM) variables on the slice [23,28],

$$\Psi_4 = C_{ij} \bar{m}^i \bar{m}^j, \qquad (22)$$

where

$$C_{ij} \equiv R_{ij} - KK_{ij} + K_i{}^k K_{kj} - \mathrm{i}\epsilon_i{}^{kl}\nabla_l K_{jk}. \qquad (23)$$

We note that the we have also implemented an independent method to compute gravitational radiation via the measurements of the nonspherical gauge-invariant metric perturbations of a Schwarzschild black hole [29–31] (A review on the basic formalism can be found in [32] and Refs. [29–31] provide examples of the applications of this method to Cartesian-coordinate grids). For compactness, hereafter we will limit our discussion to the gravitational radiation measured in terms of the curvature scalar Ψ_4.

In a similar manner, the EM radiation can be measured using the Newman-Penrose scalar Φ_2 defined as

$$\Phi_2 \equiv F^{\mu\nu} \bar{m}_\mu n_\nu, \qquad (24)$$

with the same tetrad used for Ψ_4, allowing to measure outgoing EM radiation. (Possible gauge effects, as those discussed in [33], have been seen to be negligible in [18], and the results here agree with those).

Using the curvature scalars Ψ_4 and Φ_2 it is also possible to compute the energy carried off by outgoing waves at infinity. More specifically, the total energy flux per unit solid angle can be computed directly as

$$F_{\mathrm{GW}} = \frac{dE_{\mathrm{GW}}}{dtd\Sigma} = \lim_{r\to\infty} \frac{r^2}{16\pi} \left| \int_{-\infty}^t \Psi_4 dt' \right|^2 \qquad (25)$$

$$F_{\mathrm{EM}} = \frac{dE_{\mathrm{EM}}}{dtd\Sigma} = \lim_{r\to\infty} \frac{r^2}{4\pi} |\Phi_2|^2. \qquad (26)$$

Representing now Ψ_4 and Φ_2 via a standard decomposition into spherical harmonics using the spin-weights -2 for Ψ_4 and -1 for Φ_2, we obtain the final expressions

$$F_{\mathrm{GW}} = \frac{dE_{\mathrm{GW}}}{dt} = \lim_{r\to\infty} \frac{r^2}{16\pi} \sum_{l,m} \left| \int_{-\infty}^t A^{lm} \right|^2 dt' \qquad (27)$$

$$F_{\mathrm{EM}} = \frac{dE_{\mathrm{EM}}}{dt} = \lim_{r\to\infty} \frac{r^2}{4\pi} \sum_{l,m} |B^{lm}|^2, \qquad (28)$$

where A^{lm} and B^{lm} are the coefficients of the spherical harmonic decomposition of Ψ_4 and Φ_2, respectively.

III. PHYSICAL AND ASTROPHYSICAL SETUP

As mentioned in the introduction, the astrophysical scenario we have in mind is motivated by the merger of supermassive black hole binaries resulting from galaxy mergers. More specifically, we consider the astrophysical conditions that would follow the merger of two supermassive black holes, each of which is surrounded by an accretion disc. As the merger between the two galaxies takes place and the black holes become close, a "circumbinary" accretion forms and reaches a stationary accretion phase. During this phase, the binary evolves on the timescale of the emission of gravitational radiation and its separation progressively decreases as gravitational waves carry away energy and angular momentum from the system. This radiation-reaction timescale is much longer than the (disc) accretion timescale, which is regulated by the ability of the disc to transport outwards its angular momentum (either via viscous shear or magnetically-mediated instabilities). As a consequence, for most of the evolution the disc slowly follows the binary as its orbit shrinks. However, as the binary separation becomes of the order of $\sim 10^5$–$10^6 M$, the radiation-reaction timescale reduces considerably and can become smaller than the disc accretion one. When this happens, the disc becomes disconnected from the binary, the mass accretion rate reduces substantially and the binary performs its final orbits in an "interior" region which is essentially devoid of gas [3–5]. This represents the astrophysical setup of our simple model.

We introduce a coupling between the binary and the disc via a large-scale magnetic field which we assume to be anchored to the disc, whose inner edge is at a distance of $\sim 10^3 M$ and is effectively outside of our computational domain, while the binary separation is only of $\sim 10M$, where M is the total gravitational mass of the binary. We note that although the large-scale magnetic field is poloidal, it will appear as essentially uniform within the "interior region" where the binary evolves and which we model here. As a result, the initially magnetic field adopted

has Cartesian components given simply by $B^i = (0, 0, B_0)$ with $B_0 M = 10^{-4}$ in geometric units or $B_0 \sim 10^8$ G for a binary with total mass $M = 10^8 M_\odot$. Furthermore, because we consider an electromagnetic vacuum, the charges, electric currents and the initial electric field are all assumed to be zero, i.e., $E^i = 0$.

We note that although astrophysically large, the initial magnetic field considered here has an associated EM energy which is several orders of magnitude smaller than the gravitational-field energy. As a result, any effect from the EM field dynamics on the spacetime itself will be negligible and so the EM fields are treated here as test fields. The case of stronger magnetic fields and their consequent impact on the spacetime will be presented in a forthcoming work.

IV. ISOLATED BLACK HOLES

We first study isolated black holes, both as a check of our implementation and to analyze the interaction of the chosen external initial magnetic field with the spacetime curvature generated by the black holes. The initial magnetic field in all simulations is uniform with strength B_0 and aligned with the z axis, while the initial electric field is zero everywhere. Although this solution satisfies the Maxwell equations trivially, it is not a stationary solution of the coupled Einstein-Maxwell system for the chosen black hole initial data. The solution thus exhibits a transient behavior and evolves towards a time-independent state given by a solution first found by Wald [34]. One important feature of Wald's solution is that in the case of spinning black holes, a net charge (and hence a net electric field) will develop as a result of "selective accretion" and whose asymptotic value is simply given by $Q = 2B_0 J$. Although this charge is astrophysically uninteresting, being limited to be $Q/M \le 2B_0 M \simeq 1.7 \times 10^{-20} B_0 (M/M_\odot)$ G [34] for a Kerr black hole with $J/M^2 \le 1$, it represents an excellent test bed for our numerical setup.

To validate the ability of the code to recover this analytic solution we have performed several tests involving either a Schwarzschild black hole or Kerr black holes with dimensionless spin parameters $a = J/M^2 = 0.7$ (this value chosen as it is close to the final spin values resulting from the merger simulations covered in Sec. IV). In this latter case, the spin vector was chosen to be either parallel to the background magnetic field, i.e., with $J^i = (0, 0, J)$ or orthogonal to it, i.e., with $J^i = (J, 0, 0)$. As expected, the early stages in the evolution reveal a transient behavior as the EM fields rearrange themselves and adapt to the curved spacetime reaching a stationary configuration after about $\sim 70M$. The electric field, in particular, goes from being initially zero to being nonzero and decaying radially from the black hole.

Although the original solution found by Wald was expressed in Boyer-Lindquist coordinates, there is a simple

way to validate that our gauge is sufficiently similar (at least at far distances) and that the numerical solution approaches Wald's one for an isolated black hole in a uniform magnetic field. This is shown in Fig. 1, which reports the time evolution of the EM fields E and B for a simulation of the Kerr black hole with spin $a = 0.7M$ aligned with the magnetic field. In particular, the top panel shows the time evolution of the electric field when the latter is rescaled by the radial positions where it is measured, i.e., Er^2 with $r = 4M, 8M, 16M$, and $24M$. Because of $E \propto B_o J/r^2$, one expects the different lines to be on top of each other. This is clearly the case for the data extracted at $r = 16M$ and $24M$, but it ceases to be true for the data at $r = 4M, 8M$, for which the magnetic field and gauge structure are strongly influenced by the black-hole geometry. Interestingly, however, in this strong-field region near the black hole another scaling can be found and which is closely related to one expressed by Wald's solution. In particular, the radial dependence of the magnetic field can be factored out by considering the ratio of the electric and magnetic field which, in Wald's solution should be proportional to the black-hole spin only. The bottom panel of Fig. 1 shows therefore the evolution of $(E/B)r^2 \sim J$ which is indeed a constant at all the radial positions as shown by the good overlap among the different curves. We
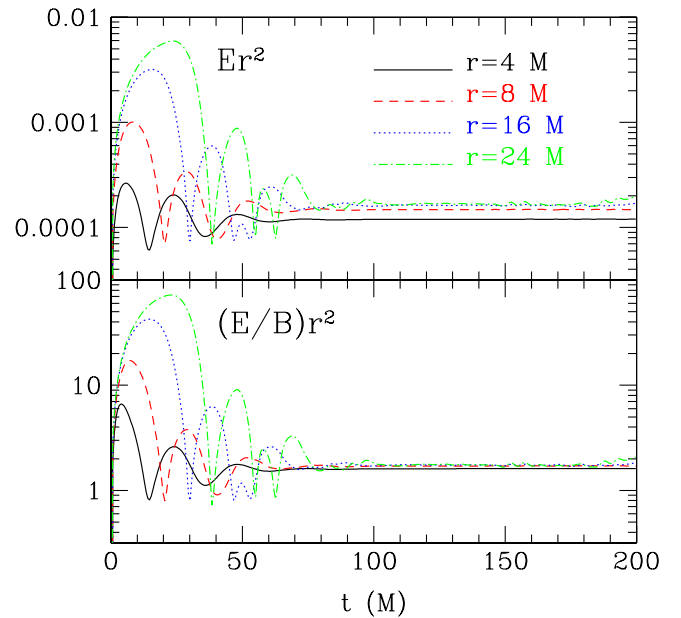

FIG. 1 (color online). Recovery of Wald's solution for an isolated Kerr black hole with dimensionless spin $a = 0.7$. Shown in the top panel are the values of the electric field as measured at different distances from the origin; since $Er^2 \sim B_0 J$, the different lines should overlap at late times if the magnetic field is uniform which is evident in the figure. Shown in the bottom panel is the ratio of the electric and magnetic fields which is proportional to the black-hole spin only. Note the transitory state until $t \approx 70M$, when the solution reaches a stationary state.
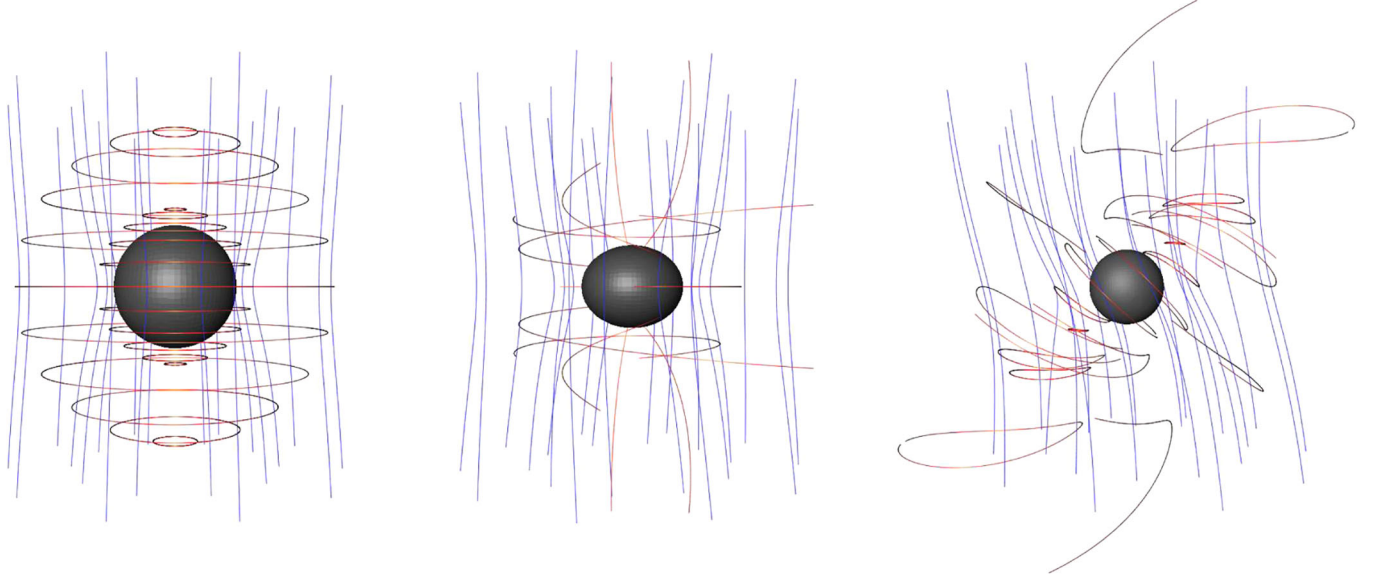
FIG. 2 (color online). Left panel: Magnetic (blue) and electric field (red/magenta) field lines at $t = 200M$ for a Schwarzschild black hole. Central panel: the same as in the left panel but for a Kerr black hole with spin $a = J/M^2 = 0.7$ aligned with the magnetic field, i.e., $J^i = \{0, 0, J\}$. Right panel: The same as in the center panel but for a Kerr black hole with spin $a = J/M^2 = 0.7$ which is orthogonal to the magnetic field, i.e., $J^i = \{J, 0, 0\}$. Indicated with black surfaces are the apparent horizons.

find that this scaling can be used as an effective test which is valid at all radial positions. These observations, together with the clear approach to a stationary configuration indicate the asymptotic (in time) behavior is indeed described by Wald's solution.

In order to obtain a more intuitive picture of the different solutions for isolated black holes, we now turn our attention to the structure of the electric and magnetic fields themselves. While those field lines are gauge-dependent, they can be used to determine the effect of the spin orientation of the black holes on the solution. Figure 2 shows
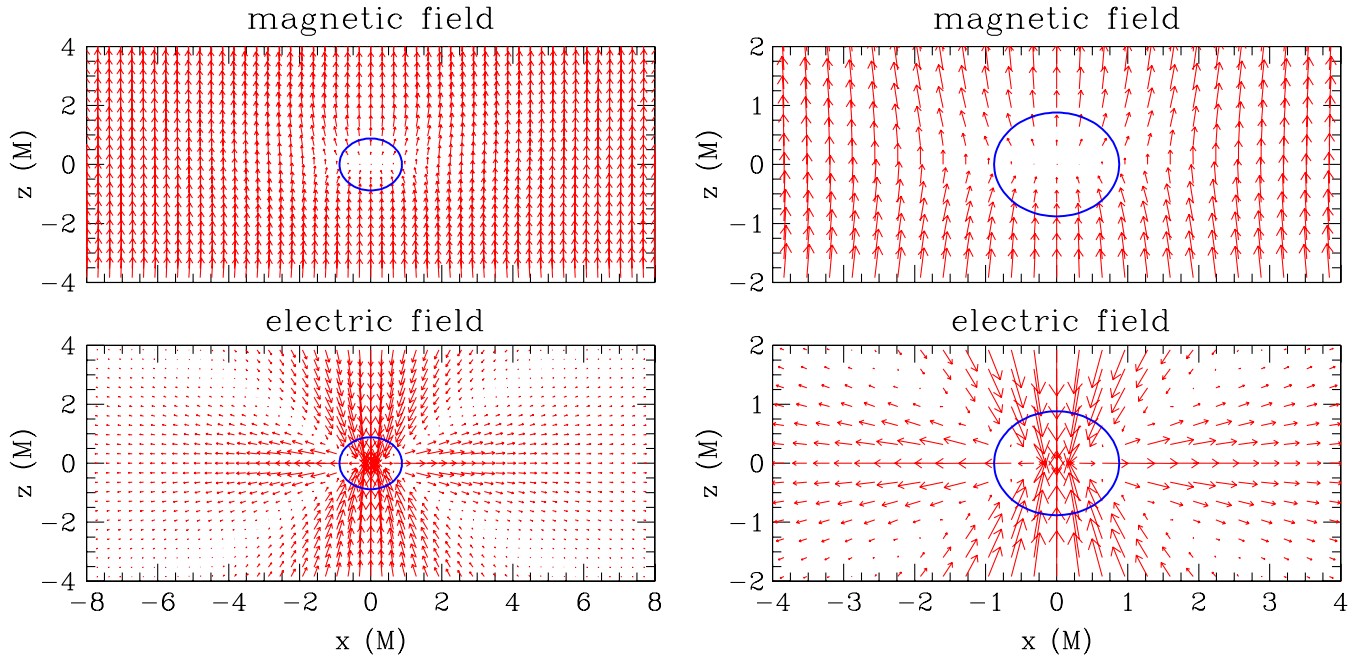

FIG. 3 (color online). Left panel: Large-scale magnetic and electric field lines on the plane $y = 0$ and at $t = 200M$ for a Kerr black hole with spin $J/M^2 = 0.7$ aligned with the magnetic field, i.e., along the z axis. Indicated with blue circles are the apparent horizons. Right panel: The same as on the left panel but on a smaller scale to highlight the fields structure in the vicinity of the black hole.

therefore the three-dimensional (3D) EM field configurations at late simulation times when the solution has settled to a stationary state for either a Schwarzschild black hole (left panel), or for Kerr black holes with spin aligned (central panel) or orthogonal to the magnetic field (right panel). Note that in all of the panels, the magnetic field lines are bent by the black hole geometry. The appearance of toroidal electric field in the case of a nonspinning black hole does not contradict Wald's solution, for which it should be identically zero. It is due to the nonvanishing radial shift vector which, when coupled with the vertical magnetic field, leads to a toroidal magnetic field [18]. Finally, note that whenever the black hole is rotating, together with the gauge-induced toroidal electric field, there appears also a poloidal component which is induced by the gravitomagnetism (or frame-dragging) of the rotating black hole and whose detailed geometry depends on the relative orientation of the spin with respect to the background magnetic field. For compactness we do not report here the EM field configuration for a rotating black hole with spin antialigned with respect to the magnetic field. It is sufficient to remark that the solution shows the same behavior as the aligned case, with a simple reversal in the direction of the spin-induced effects.

To gain some insight on the influence of the black-hole spin and orientation on the EM field lines, it is useful to exploit the phenomenological description offered by the "membrane paradigm" [35]. In such approach, the horizon of a rotating black hole is seen as a one-way membrane with a net a surface charge distribution which, for the case

of aligned spin and magnetic field, has negative values around the poles while positive ones around the equator. The resulting behavior is therefore the one shown in Fig. 3, where the magnetic and electric-field lines for the Kerr black hole with spin aligned with the magnetic field are presented on the $y = 0$ plane. The left panel, in particular, offers a large-scale view of the EM fields, which is however magnified on the right panels to highlight the behavior of the fields near the apparent horizons. Finally, shown in Fig. 4 are the magnetic and electric-field lines on the $y = 0$ plane for the Kerr black hole with spin orthogonal to the magnetic field, i.e., along the x axis. Note that while the differences in the magnetic field configurations in Fig. 3 and 4 are small and difficult to observe even in the zoomed-in version of the figures, the differences in the electric fields are instead significant and related to the different spin orientations.

V. BINARY BLACK HOLES

We next extend the considerations made in the previous section to a series of black-hole binaries having equal masses and spins that are either aligned or antialigned with the orbital angular momentum.

A. Initial data and grid setup

We construct consistent black-hole initial data via the "puncture" method as described in Ref. [36]. We consider equal mass binaries with four different spin configurations belonging to the sequences labeled as "r" and "s" along
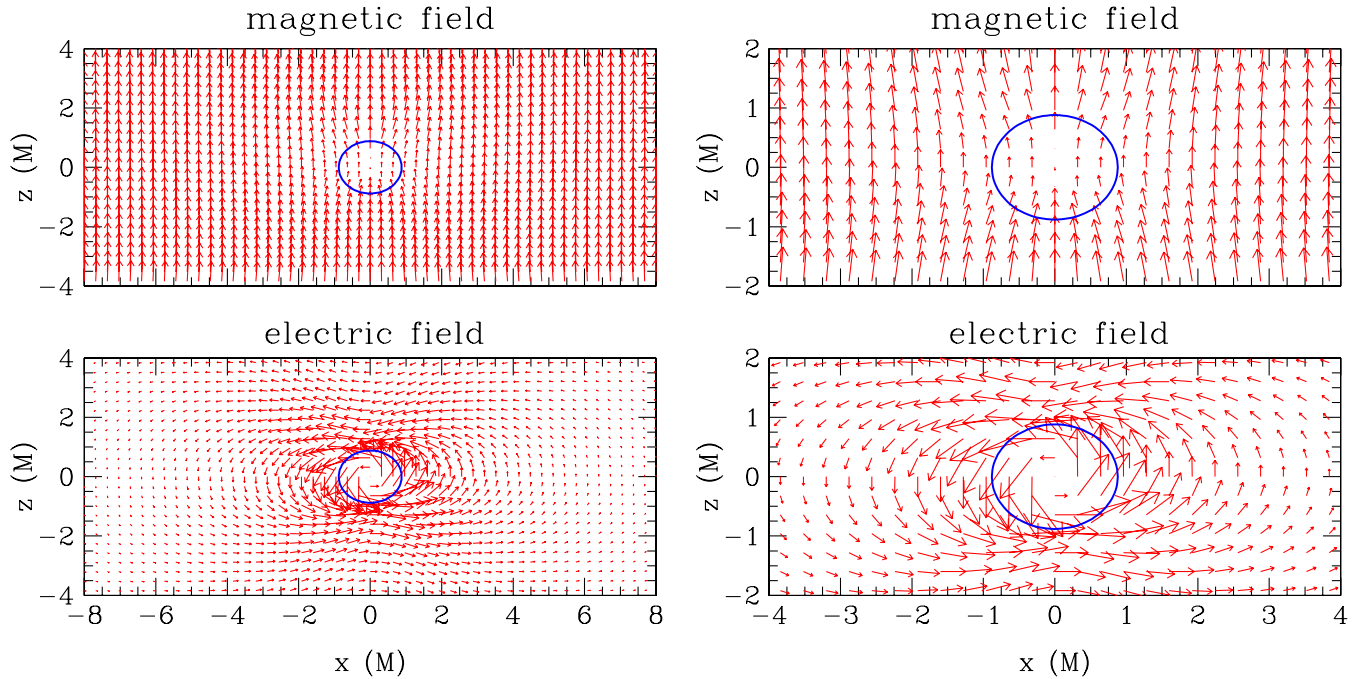

FIG. 4 (color online).   Left panel: Large-scale magnetic and electric-field lines on the plane $y = 0$ and at $t = 200M$ for a Kerr black hole with spin $J/M^2 = 0.7$ orthogonal to the magnetic field, i.e., along the x axis. Indicated with blue circles are the apparent horizons. Right panel: The same as on the left panel but on a smaller scale to highlight the fields structure in the vicinity of the black hole.

straight lines in the (a_1, a_2) parameter space, also referred to as the "spin diagram" [37,38]. These configurations allow us to cover the basic combinations for the alignment of the spin of the individuals black holes with respect to the magnetic field, while keeping the dimensionless spin parameter of the single black holes constant among the different binaries considered. Furthermore, it allows us to study the impact that the final black hole spin has on the late stages of the merger.

We note that similar sequences have also been considered in [39–43] but have here been recalculated both using a higher resolution and with improved initial orbital parameters. More specifically, we use post-Newtonian evolutions following the scheme outlined in [44], which provides a straightforward prescription for initial-data parameters with small initial eccentricity, and which can be interpreted as part of the process of matching our numerical calculations to the inspiral described by the post-Newtonian approximations. The free parameters of the puncture initial data we fix are: the puncture coordinate locations Ci, the puncture bare mass parameters m_i, the linear momenta pi, and the individual spins Si. The initial parameters for all of the binaries considered are collected in Table I. The initial separations are fixed at $D = 8M$ with the exception of the s_{-6} binary having an initial separation of $D = 10M$. Here M is the total initial black-hole mass, chosen as $M = 1$ (note that the initial ADM mass of the spacetime is not exactly 1 due to the binding energy of the black holes), while the individual asymptotic initial black-hole masses are therefore $M_i = 1/2$. In addition, we choose the initial parameters for the EM fields to be $B^i = (0, 0, B_0)$ with $B_0 \sim 10^{-4}/M \sim 10^8(10^8 M_\odot/M)$ G and $E^i = 0$. The setup for the numerical grids used in the simulations consists of 9 levels of mesh refinement with a fine-grid resolution of $\Delta x/M = 0.02$ together with fourth-order finite differencing. The wave-zone grid has a resolution of $\Delta x/M = 0.128$ and extends from $r = 24M$ to $r = 180M$, in which our wave extraction is carried out. The outer (coarsest) grid extends to a spatial position which is $819.2M$ in each coordinate direction.

B. Binary evolution and spin dependence

As mentioned above, we consider configurations where both black holes have equal mass and the individual black-hole spins are either aligned or antialigned with the mag-

netic field (and orbital angular momentum). We thus consider a set of three different spinning binaries, as well as a nonspinning binary, which we take as a reference (cf. Table I).

One feature of our simulations, that was already analyzed for single black holes in Sec. IV, and is of even greater interest for binaries, is the structure of the EM field lines induced by the spacetime dynamics around the black holes. The fieldline configurations, in fact, change considerably throughout the course of our simulations. When there is a large separation between the orbiting black holes, the electric field structure in both nonspinning and spinning binary systems is dominated by the orbital motion of the individual black holes. In particular, an inspection of the electric field vector along a line joining their centers indicates an outward radial dependence. This can be understood from the phenomenological interpretation suggested by the membrane paradigm and has been observed already in [18]. Namely, as the black holes move in a direction which is essentially orthogonal to the magnetic field, an effective quadrupolar charge separation develops on the horizons with effective positive charges at the poles and negative ones on the equator, thus inducing an electric field emanating from each black hole. This induced quadrupolar electric field is therefore reminiscent of the one produced by a conductor moving through a uniform magnetic field as the result of the Hall effect.

It is interesting to note that while the differences in the magnetic field lines among the various binaries considered are rather small, the differences in the electric fields show significant variation across the spin configurations. This is illustrated in Fig. 5, which shows the electric field lines at different scales of interest with respect to the black holes for two spinning binary black hole systems and the nonspinning binary on the $y = 0$ plane. Here we choose to concentrate on the configurations with the spins up and up (i.e., s_6) and with the spin up and down (i.e., r_0) since the configuration with the spins down and down (i.e., s_{-6}) shows the same fieldline structure as the up and up case. In particular, the left panel of Fig. 5 reports the fieldline structure on a scale which is much larger than that of the horizons and that clearly shows the quadrupolar nature of the field. At the same time, the right panel offers a magnified view of the same binaries on scales which is comparable with those of the horizons. In this way it is possible to

TABLE I. Binary sequences for which numerical simulations have been carried out, with various columns referring to the puncture initial location $\pm x/M$, the mass parameters m_i/M, the dimensionless spins a_i, the initial momenta and the normalized ADM mass $\tilde{M}_{\rm ADM} \equiv M_{\rm ADM}/M$ measured at infinity. (See Refs. [37,38] for a discussion of the naming convention).

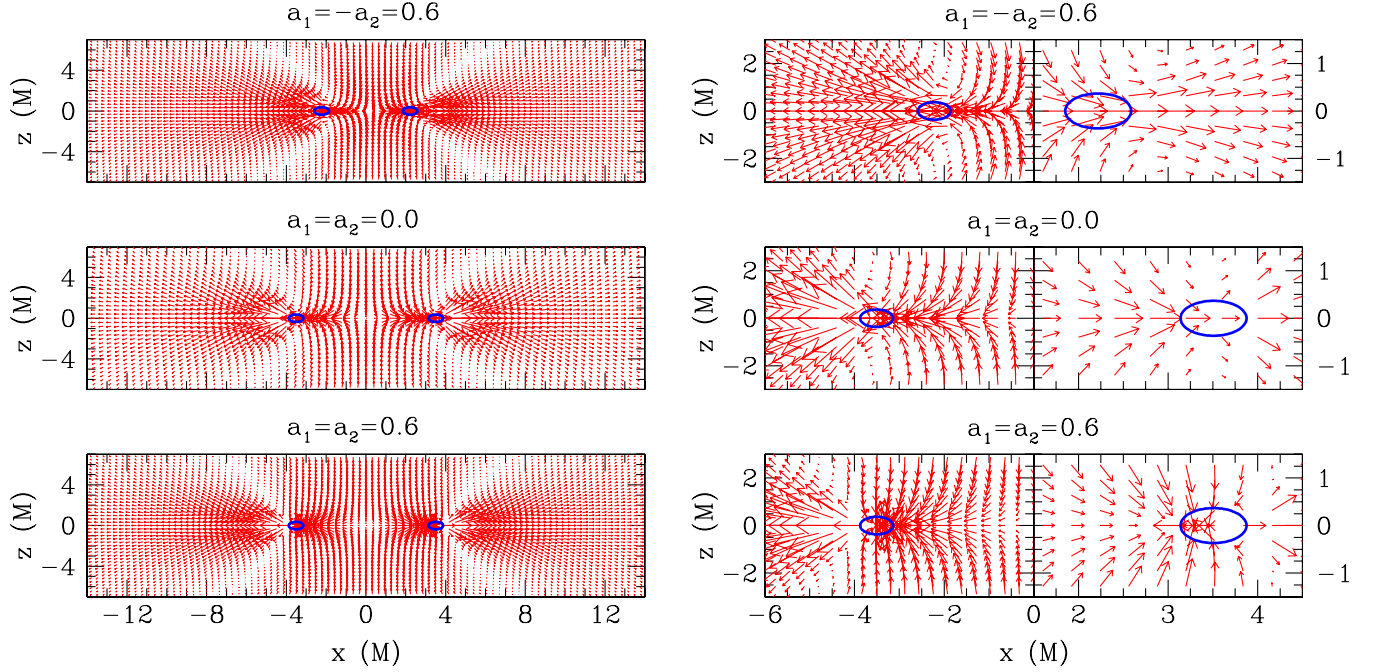|	$\pm x/M$	m_1/M	m_2/M	a_1	a_2	$(p_x, p_y)_1 = -(p_x, p_y)_2$	$\tilde{M}_{\rm ADM}$
s_{-6}	5.0000	0.4000	0.4000	-0.600	-0.600	$(0.001\,191, -0.100\,205)$	0.9873
r_0	4.0000	0.4000	0.4000	-0.600	0.600	$(0.001\,860, -0.107\,537)$	0.9865
s_0	4.0000	0.4824	0.4824	0.000	0.000	$(0.002\,088, -0.112\,349)$	0.9877
s_6	4.0000	0.4000	0.4000	0.600	0.600	$(0.001\,860, -0.107\,537)$	0.9876

FIG. 5 (color online).   Electric-field lines on the plane $y = 0$ for the r_0, s_0, and s_6 configurations at $t = 123$, 155, and 246M, respectively. Left panel: Large-scale structure of the EM fields around the apparent horizons (blue circles). Right panel: The same as on the left but on a smaller scale to highlight the field structure in the vicinity of the black holes. Note that an additional magnification is applied to the black hole "on the right" so as to highlight the change of sign in the electric field near the horizon, i.e., at $x \simeq 3M$.

find the properties of the electric field already discussed in Sec. IV for isolated black holes also in case of binary black holes. Additionally the various spin configurations lead to different small-scale properties of the field. More specifically, while the field lines of the r_0 and s_0 configurations have a similar structure even in the magnified plot, the binary with the aligned spins s_6 shows a more complex structure in which the electric field changes sign near but outside the horizon, namely, at $x \simeq 3M$ and which corresponds approximately to a distance $d \sim 2r_{\mathrm{AH}}$, with r_{AH} the mean radius of the apparent horizon. This additional property of the electric field could be related to the location of the ergosphere (which has not been computed in these simulations) and may be seen as a response of the electric field to the additional charge separation induced on the black hole horizon and which leads to a greater distortion and twisting of the field lines in this region.

Although it is not trivial to disentangle how much of this behavior of the electric field depends on the gauges used, the complex structure of the electric fields, and which varies considerably through the late inspiral and the merger of the binary, may lead to interesting dynamics and to the extraction of energy via acceleration of particles along open magnetic field lines or via magnetic reconnection. To better illustrate the complex field structure, Fig. 6 offers 3D views of both the electric and magnetic fields for the s_6 binary. In particular, in the left panel of Fig. 6 we show the electric and magnetic field lines as well as the apparent horizons when the binary is inspiraling (i.e., at $t = 328M$)

and again observe the superposition of two effects: the overall orbital motion of the black holes causing the large-scale structure of the electric field lines (highlighted in a magenta color); and the effect of the black-hole spin (in red), which causes additional dragging in the electric field lines close to the apparent horizons. In the right panel, on the other hand, we present the late-time (i.e., at $t = 690M$) state of the solution which, as expected, agrees well with the fieldline configurations presented for the Kerr black hole with spin aligned with the magnetic field in Sec. IV.

We next switch our attention to discussing how the different black hole spin configurations affect the emission of EM radiation. This requires a careful analysis of the radiative properties of the solution in both the EM and gravitational channels. We first focus on the two types of waveforms and Fig. 7 illustrates the correlation between the two emissions by showing the time-retarded waveform of the principal mode, i.e., the $\ell = m = 2$ of the spin-weighted spherical harmonic basis (note that Ψ_4 and Φ_2 have spin weight -2 and -1, respectively), for all different spin configurations to compare gravitational and EM waveforms directly. While both EM and GW radiation show the same characteristics in the dominant mode, we note that small differences arise when comparing the waveforms of the individual spin configurations more carefully with each other in the two channels. Note that the waveform for the binary s_{-6} has a larger number of cycles only because it merges very rapidly (the total angular momentum is
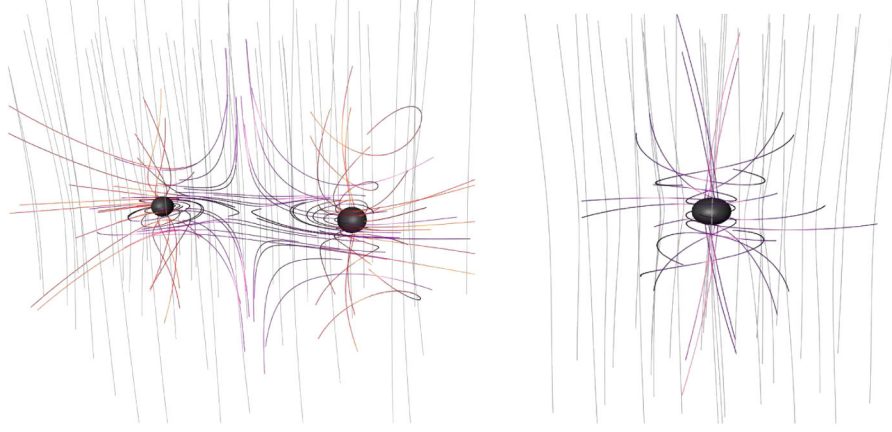
FIG. 6 (color online).　Electric (red/magenta) and magnetic-field lines (gray) in 3D for the s_6 binary during inspiral when both black holes are still far separated at time $t = 328M$ (left panel), and after the merger at $t = 690M$ (right panel).

smaller because the total spin is antiparallel to the orbital angular momentum) and thus it has been evolved from a larger initial separation $D = 10M$; all the other binaries have the same initial separation $D = 8M$. A closer inspection of Fig. 7 reveals that the amplitude evolution of the $\ell = m = 2$ mode for the different spin configurations differs when compared in the two channels. As an example, while in the GW channel the amplitude in the $\ell = 2, m = 2$ mode decreases when going from the r_0 configuration over to the s_0 and s_{-6} configurations, the amplitude remains nearly constant in the EM channel. This reveals that there are additional contributions in the EM emission coming from the higher-order modes (see Fig. 9 and the discussion below)

To further evaluate the correlation between the EM and the gravitational radiation, we now turn our attention to the amplitude and phase evolution of the main contributing spherical harmonic modes. Since radiated energy fluxes are given by Φ_2 and the time integral of Ψ_4 we here compare Φ_2 with $\tilde{\Psi}_4 \equiv \int_\infty^t \Psi_4 dt'$. For briefness we only highlight the results obtained for the s_6 configuration, since this shows the highest amount of energy being radiated in both EM and GWs, and because our remarks apply also to the other configurations. Since the main contributions to the radiated energy in the EM channel arise from the $\ell = 2, 3, 4, m = 2$ modes, we limit our analysis in this section to those modes only. In order to obtain a better understanding of the correlation in the radiation coming from the two channels, we analyze the amplitude and phase of the main contributing modes individually. Figure 8 shows the amplitude and phase evolution of the $\ell = 2, 3, m = 2$ modes in both channels. Clearly, the $\ell = m = 2$ modes show the same phase evolution (cf. the left panels) in the two forms of radiation, as expected given that the EM emission is essentially driven by the orbital motion of the binary. Furthermore, the amplitude evolution in the $\ell = 2,$
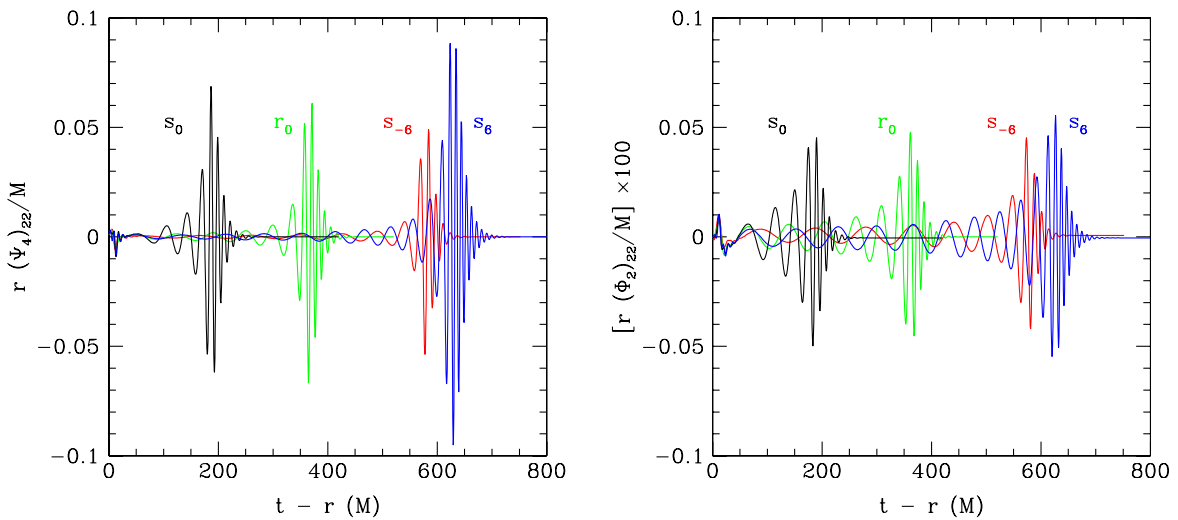

FIG. 7 (color online).　Left panel: GWs as computed from the (2, 2) mode of Ψ_4 for the different binaries reported in Table I. Right panel: The same as in the left panel but for the EM waveform as computed from Φ_2.

$m = 2$ modes of both emissions are also simply related by a constant, time-independent, factor.

Although a simple scaling factor in the evolution of $\tilde{\Psi}_4$ and Φ_2 appears for all of the different binary configurations considered here, this factor is not the same across different spin configurations. However, because the $\ell = m = 2$ represents by and large the most important contribution to the radiation emitted in the two channels and because the GW emission from binaries with spins aligned and antialigned with the orbital angular momentum has been computed in a number of related works [39–43,45–54], the results found here allow us to simply extend all of the phenomenology reported so far for the $\ell = 2$, $m = 2$ GW emission from the above cited works also to the EM channel.

Unfortunately, the tight correlation found in the amplitude evolution of the lowest-order mode disappears for higher-order modes. This is reported in the bottom panels of Fig. 8, which indicate that while the phase amplitude remains the same (cf. the bottom right panel), the evolution of the amplitude in the two channels does not differ only by a simple constant scaling factor (cf. the bottom left panel).
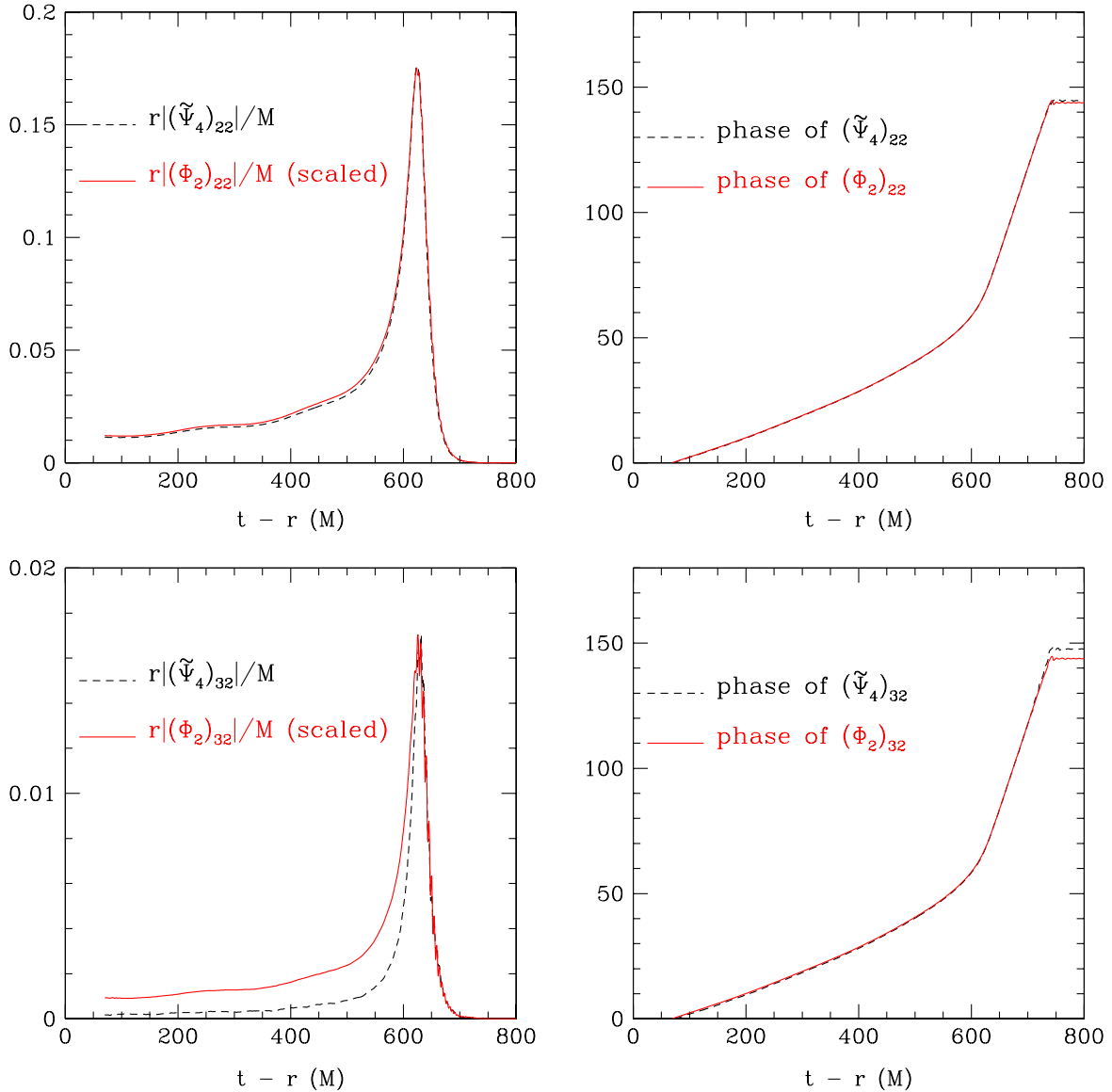

FIG. 8 (color online).   Amplitude and phase evolution of the main $\ell = m = 2$ modes for the Weyl scalar Φ_2 and the first time integral of Ψ_4 (i.e., $\tilde{\Psi}_4$), relative to the s_6 configuration. The plots show the data in retarded time $t - r$ for a detector located at $r = 100M$. While the $\ell = m = 2$ modes show the same amplitude (up to a scale factor) and phase evolution, this does not apply to modes with higher ℓ. For the $\ell = 3$, $m = 2$ and $\ell = 4$, $m = 2$ modes, the phase evolution is still identical but the amplitude no longer does not differ only by a constant scale factor.
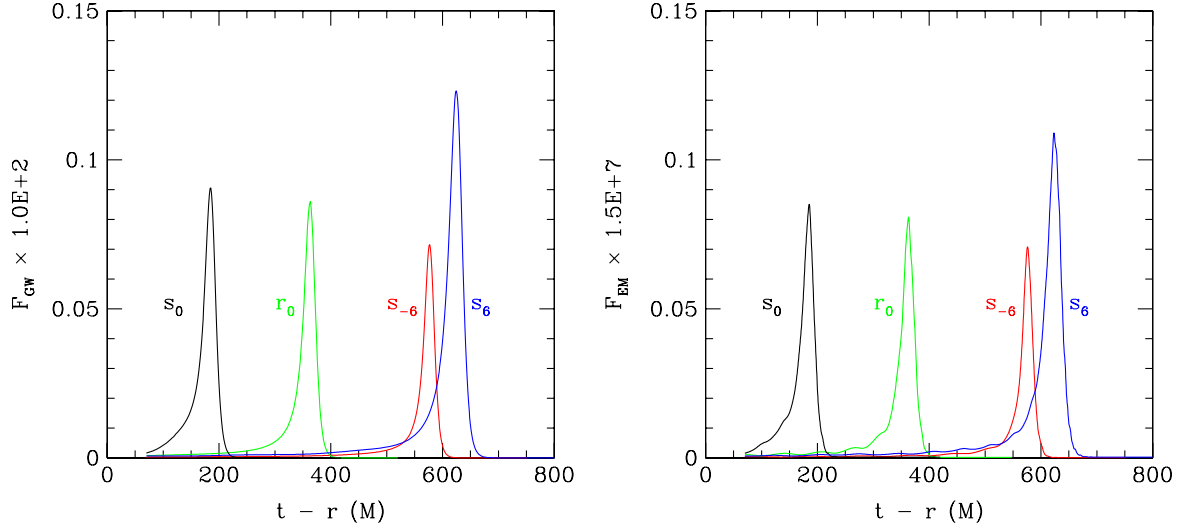
FIG. 9 (color online).   The total energy flux per unit solid angle in terms of GW waves (left panel) and of EM waves (right panel); clearly they differ only up to a scaling factor. The different lines refer to the different binaries reported in Table I.

A similar behavior is found for lower-order modes such as the $\ell = 4$, $m = 2$ one but is not reported here for compactness. Overall, these results suggest that although the main (and lowest-order) contribution to the EM emission does indeed come as a result of the dragging of the EM fields by the orbital motion of the binary, additional contributions arise from higher-order modes which are not directly related to the orbital motions. These are likely to be the result of the complex interactions among the EM fields, discussed in Fig. 5 and whose investigation, although of great interest, goes beyond the scope of this paper.

Another interesting quantity to consider in our analysis is the energy carried away from the systems in the two emissions, which can be computed by using Eqs. (27) and (28), where we have taken into account modes up to $\ell = 4$. Despite the differences between the EM and gravitational waves discussed already, when looking at the emission in the lowest-order modes that can be associated to the different multipolar decomposition of the two emissions (cf. Fig. 7), we find that the overall energy fluxes are extremely similar and differ essentially only by a constant (but large) factor. This is shown in Fig. 9 which reports both the GW (left panel) and the EM radiated energy fluxes (right panel) when integrated over a sphere located at $r = 100M$ for all the binary sequences considered here. Once again, the fact that $F_{\rm EM}$ basically mimics $F_{\rm GW}$, underlines that the emission in the EM channel is intimately tied to the emission in GW, so that the observation of one of the two would lead to interesting information also about the other one. As a final comment it is worth noting that although the energy fluxes from the binaries s_0 and r_0 show a different evolution, the total emitted energy, namely, the area under the curves, is extremely similar and is reported in Table II. This provides yet an additional confirmation of the results already presented in Refs [38,41–43,54] for binaries with aligned

spins and yields further support to the conjecture that when the initial spin vectors are equal and opposite and the masses are equal, the overall dynamics of the binary is the same as that of the corresponding nonspinning binary.

VI. ASTROPHYSICAL DETECTABILITY

As discussed in the previous sections, the EM and GW radiation are tightly coupled and evolve on exactly the same timescales and with the same spectral distribution in frequency. The *rates* of loss of energy and angular momentum, however, are very different. This is summarized in Table II which reports the total energy radiated during the inspiral and merger in either EM waves or GWs (i.e., $E_{\rm EM}^{\rm rad}/M$, $E_{\rm GW}^{\rm rad}/M$) and the angular momenta radiated in GWs (i.e., $J_{\rm GW}^{\rm rad}/M^2$). From the values obtained, two interesting observations can be made. The first one is that the radiated EM energy is higher for binaries which lead to a more highly spinning final black hole. This is a consequence of these binaries merging with increasingly tighter orbits and at higher frequencies, which leads to stronger EM and GW fluxes. The second one has already been mentioned in the previous Section and reflects the fact that the binaries r_0 and s_0 lead to the same energy emission

TABLE II.   Relative emitted energies in EM waves and GWs ($E_{\rm EM}^{\rm rad}/M$, $E_{\rm GW}^{\rm rad}/M$, respectively), and emitted angular momentum in GWs ($J_{\rm GW}^{\rm rad}/M^2$), for the magnetic field $B_0 M = 10^{-4}$.

model	$E_{\rm EM}^{\rm rad}/M$	$E_{\rm GW}^{\rm rad}/M$	$J_{\rm GW}^{\rm rad}/M^2$
s_{-6}	1.562E − 7	0.0243	0.216
r_0	2.040E − 7	0.0357	0.213
s_0	2.055E − 7	0.0354	0.243
s_6	3.412E − 7	0.0590	0.380

(and to the same final black-hole spin [41–43,54]) despite the s_0 binary has black holes with nonzero individual spins.

Note also that, in contrast with the losses in the GW emission, those in the EM one do not depend just on the masses and initial spins of the black holes but also on the strength of the initial magnetic field. This dependence must naturally scale quadratically with the magnetic field, so that we can write

$$\frac{E_{\rm EM}^{\rm rad}}{M} = k_1(a_1, a_2, M_1, M_2)B_0^2 \tag{29}$$

$$= 1.43 \times 10^{-32} k_1 \left(\frac{M}{M_\odot}\right)^2 \left(\frac{B}{1\mathrm{G}}\right)^2, \tag{30}$$

where we have used the following relation

$$B[\mathrm{G}] = 8.36 \times 10^{19}\left(\frac{M_\odot}{M}\right)B[\mathrm{geom.\,units}]. \tag{31}$$

to convert a magnetic field in geometric units ($B[\mathrm{geom.\,units}]$) into a magnetic field expressed in Gauss ($B[\mathrm{G}]$).

As discussed before, the EM emission is closely related via simple scaling factors to the GW one and whose efficiency has been discussed in detail in Sec. VB of Ref. [38]. In particular, it was shown there that the radiated GW energy depends quadratically on the total dimensionless spin [see Eq. (24) in [38]] and the corresponding coefficients $\tilde{p}_i$ were presented in Eq. (25) in the same reference. Hence, at least in the case of equal-mass binaries, it is trivial to express $k_1(a_1, a_2, M_1, M_2)$ in terms of the suitably rescaled coefficients $\tilde{p}_i$ in [38]. Here, however, because we are interested in much simpler order-of-magnitude estimates, we will neglect the dependence of k_1 on the spins and simply assume that $k_1 \sim 10^{-7}$, so that

$$\frac{E_{\rm EM}^{\rm rad}}{M} \simeq 10^{-15}\left(\frac{M}{10^8 M_\odot}\right)^2\left(\frac{B}{10^4\mathrm{G}}\right)^2, \tag{32}$$

where we have considered a total black-hole mass of $10^8 M_\odot$ and a magnetic field of 10^4 G as representative of the one possibly produced at the inner edges of the circumbinary disc [55] [see [56] for a recent discussion on the strength of magnetic fields in active galactic nuclei (AGN)].

It should be noted that only when an extremely strong magnetic field of $\sim 10^{11}$ G is considered, does the EM efficiency become as large as $E_{\rm EM}^{\rm rad}/M \simeq 10^{-1}$ and thus comparable with the GW one. For more realistic magnetic fields, however, and assuming for simplicity that $E_{\rm GW}^{\rm rad}/M \sim 10^{-2}$ for all possible spins, the ratio of the two losses is

$$\frac{E_{\rm GW}^{\rm rad}}{E_{\rm GW}^{\rm rad}} \simeq 10^{-13}\left(\frac{M}{10^8 M_\odot}\right)^2\left(\frac{B}{10^4\mathrm{G}}\right)^2. \tag{33}$$

That is, for a realist value of the initial magnetic field, the GW emission is 13 orders of magnitude more efficient than

the EM one. More importantly, however, the frequency of variation of the EM fields is of the order

$$f_{\rm B} \simeq (40M)^{-1} \simeq 10^{-4}\left(\frac{10^8 M_\odot}{M}\right)\mathrm{Hz} \tag{34}$$

and therefore much lower than what is accessible via astronomical radio observations, which are lower-banded to frequencies of the order of ~ 30 MHz. As a result, it is very unlikely that a *direct* observation of the induced EM emission would be possible even from this simplified scenario.

Nevertheless, in the spirit of assessing whether this large release of EM radiation can lead to *indirect* observations of an EM counterpart, it is useful to compare $E_{\rm EM}^{\rm rad}$ with the typical luminosity of an AGN. To fix the ideas let us consider again a black hole of mass $M = 10^8 M_\odot \simeq 10^{41}$ g $\simeq 10^{61}$ erg, so that the luminosity in EM waves for $B_0 = 10^4$ G will be

$$L_{\rm EM} \equiv \frac{E_{\rm EM}^{\rm rad}}{\tau} \simeq 10^{41}\left(\frac{B}{10^4\,\mathrm{G}}\right)^2 \mathrm{erg\,s}^{-1} \simeq 10^8\left(\frac{B}{10^4\,\mathrm{G}}\right)^2 L_\odot,$$

$$\simeq 10^{-4}\left(\frac{B}{10^4\,\mathrm{G}}\right)^2 L_{\rm Edd}, \tag{35}$$

where we have assumed a timescale $\tau \simeq 10^3 M \simeq 10^5$ s $\simeq$ 1d and where $L_\odot$, $L_{\rm Edd}$ are the total luminosity of the Sun and the Eddington luminosity $L_{\rm Edd} = 3.3 \times 10^4 (M/M_\odot)L_\odot$, respectively. While this is a rather small luminosity (distant quasars are visible with much larger luminosities of the order 10^{47} erg s^{-1}), it is comparable with the luminosity of nearby AGNs and that is of the order of 10^{41} erg s^{-1}. More important, however, is the comparison between the EM emitted by the merging binary and the one coming from the accretion disc. Using (35) it is straightforward to deduce that the binary EM luminosity is comparable with that of an AGN accreting at 10^{-4} the Eddington rate. Hence, unless the accretion rate is rather small (namely, much smaller than 10^{-4} the Eddington rate with the extreme case being the nonaccreting scenario) the EM emission from the binary would be not only restricted to very low frequencies but also just a small fraction of the total luminosity. Under these conditions it is unlikely that such emission could have an observable impact on the overall luminosity of the accreting system.

As a final consideration it is useful to estimate whether the inspiraling binary could nevertheless imprint a detectable effect on the disc via the perturbations in the magnetic field it can produce. To assess whether this is the case we first compare the frequency $f_{\rm B}$ with the typical plasma frequency

$$f_{\rm P} = \frac{\omega_{\rm P}}{2\pi} = \left(\frac{n_e e^2}{\pi m_e}\right)^{1/2} \simeq 10^{14}\left(\frac{n_e}{10^{21}\,\mathrm{cm}^{-3}}\right)\mathrm{Hz}, \tag{36}$$

where n_e is the electron number density, or with the electron cyclotron $f_{\rm C}$ frequency

$$f_{\mathrm{C}} = \frac{\omega_{\mathrm{C}}}{2\pi} = \frac{eB}{2\pi m_e c} \simeq 10^{10}\left(\frac{B}{10^4\,\mathrm{G}}\right)\,\mathrm{Hz}. \qquad (37)$$

Clearly, the magnetic field varies with a frequency f_B that is between 14 and 18 orders of magnitude smaller and hence that the electrons and protons in the disc are always able to "adjust" themselves to the changes in the magnetic fields, which are extremely slow when compared with the typical timescales in the plasma. Stated differently, the EM radiation produced by the inspiral cannot penetrate the disc and will be effectively reflected over a skin depth of $\lambda = c/\omega_e \simeq 8 \times 10^{-6}$ cm.

Finally, we consider whether the perturbed magnetic field can have impact on the transport of angular momentum in the disc and hence modify its accretion rate in a detectable way. It is worth remarking, in fact, that there is considerably large EM energy flux reaching the accretion disc and that is $F_{\mathrm{EM}} \simeq L_{\mathrm{EM}}/r_{\mathrm{in}}^2 \sim 10^{11}(B/10^4\,\mathrm{G})^2 \mathrm{erg\,s^{-1}\,cm^{-2}}$, where $r_{\mathrm{in}} \sim 10^2 r_g$ is the inner radius of the disc and $r_g \simeq 10^{15}$ cm is the gravitational radius for a black hole of $10^8 M_\odot$. A crude way to estimate the perturbation on the disc is by considering the ratio between the viscous transport timescale τ_V and the magnetic transport timescale induced by the oscillating magnetic field, τ_B. Should this ratio be of the order of unity (or larger), then the magnetic-field perturbation may be transmitted to the disc in the form of Alfvén waves. In practice we estimate this by considering the (inverse) ratio between the viscous and magnetic torques, with the first one being expressed in terms of the average pressure p and sound speed c_s as $f_{\phi,V} \simeq \alpha p \simeq \alpha \rho c_s^2$ and the second one as $f_{\phi,B} \simeq r\delta B^\phi B^z \alpha/(8\pi) \simeq r\beta B_0^2/(8\pi)$; here α is the standard alpha-disc viscosity parameter and β is a measure of the perturbation induced in the background magnetic field (i.e., $\delta B^\phi \sim \beta B_0$, $B^z \sim B_0$). We therefore obtain

$$\frac{\tau_V}{\tau_B} = \frac{f_{\phi,B}}{f_{\phi,V}}$$

$$\simeq 10\frac{\beta}{\alpha}\left(\frac{r}{10^{-2}r_g}\right)\left(\frac{10^{-2}\,\mathrm{g\,cm^{-3}}}{\rho}\right)\left(\frac{B_0}{10^4\,\mathrm{G}}\right)^2\left(\frac{c}{c_s}\right)^2, \qquad (38)$$

where $10^{-2}r_g$ is the typical length scale over which magnetic torques could operate. Assuming now $\alpha \simeq 0.1 - 0.01$, $\beta \sim 10^{-2}$, and $c_s 0.1 - 0.01c$ as reference numbers, the rough estimate (38) suggests that it is indeed possible that $\tau_V > \tau_B$ and hence that the perturbations in the magnetic field, albeit small and rather slow, can induce a change in the viscous torque and hence induce a change in the accretion rate if the latter is sufficiently stable. Determining more precisely whether this modulation in the magnetic field can effectively leave an imprint on the accretion flow would require a more accurate modeling of the accretion disc and is clearly beyond the scope of this

simple estimate. It is however interesting that this possibility is not obviously excluded.

In summary, the analysis carried out in this Section shows that it is highly unlikely that the EM emission associated with the scenario considered in this paper can be detected *directly* and simultaneously with the GW one. This is essentially because the EM is too inefficient for realistic values of the magnetic fields and because it operates at frequencies which are well outside the ones accessible to astronomical radio observations. However, if the accretion rate of the circumbinary disc is sufficiently stable over the timescale of the final inspiral and merger of the black-hole binary, then it may be possible that the EM emission will be observable *indirectly* as it will alter the accretion rate through the magnetic torques exerted by the distorted magnetic field lines. A firmer conclusion of whether this can actually happen in practice will inevitably have to rely on a more realistic description of the accretion process.

As a final comment we stress that our analysis and discussions have not included the role of gas or plasmas around the black hole(s) nor have we considered resistive scenarios. Both of these ingredients, when coupled to the EM fields behavior described here, could induce powerful emissions by accelerating charged particles via the strong fields produced (e.g., in a manner similar to the Blandford-Znajek mechanism [16]) or by affecting the gas or plasmas dynamics or via the reconnection of the complex EM fields produced during the inspiral and merger. Future work in these directions is needed in order to shed light on these possibilities and assess their realistic impact as EM counterparts to the GW emission.

VII. CONCLUDING REMARKS

We have analyzed the phenomenology that accompanies the inspiral and merger of black-hole binaries in a uniform magnetic field which is assumed to be anchored to a distant circumbinary disc. Our attention has been concentrated on binaries with equal masses and equal spins which are either aligned or antialigned with the orbital angular momentum; in the case of supermassive black holes, these configurations are indeed expected to be the most common ones [19,20]. Furthermore, this choice allows us to disentangle possible precession effects and concentrate on the EM fields dynamics as affected by the orbital motion of the binary. Overall, the simulations reveal several interesting aspects in the problem:

(i) The orbital motion of the black holes distorts the essentially uniform magnetic fields around the black holes and induces a quadrupolar electric field analogous to the one produced by the Hall effect for two conductors rotating in a uniform magnetic field. In addition, both electric and magnetic fields lines are dragged by the orbital dynamics of the binary. As a result, a time variability is induced in the EM fields,

which is clearly correlated with the orbital behavior and ultimately with the GW emission. The EM fields become, therefore, faithful tracers of the spacetime evolution.

(ii) As a result of the binary inspiral and merger, a net flux of electromagnetic energy is induced which, for the $\ell = 2$, $m \pm 2$ modes is intimately tied, via a constant scaling factor in amplitude, to the gravitational energy released in GWs. This specular behavior in the amplitude evolution disappears for higher order modes, even though the phase evolution remains the same for all modes.

(iii) Because the tight correlation between the EM and the GW emission has been found for all of the cases considered here, we expect it to extend to all possible binary configurations as long as the EM fields are playing the role of "test fields". Hence, the modelling of the GW emission does in practice provide information also on the EM one within the scenario considered here.

(iv) Although the global *large-scale* structure of the EM fields is dictated by the orbital motion, the individual spins of the black holes further distort the EM field lines in their vicinities. These *small-scale* fields may lead to interesting dynamics and to the extraction of energy via acceleration of particles along open magnetic-field lines or via magnetic reconnection.

(v) The energy emission in EM waves scales quadratically with the total spin and is given by $E_{\rm EM}^{\rm rad}/M \simeq 10^{-15}(M/10^8 M_\odot)^2 (B/10^4 \text{ G})^2$, thus being 13 orders of magnitude smaller than the gravitational energy for realistic magnetic fields. This EM emission is at frequencies of $\sim 10^{-4}(10^8 M_\odot/M)$ Hz, which are well outside those accessible to astronomical radio observations. As a result, it is unlikely that the EM emission discussed here can be detected *directly* and simultaneously with the GW one.

(vi) Processes driven by the changes in the EM fields could however yield observable events. In particular we argue that if the accretion rate of the circumbinary disc is small and sufficiently stable over the timescale of the final inspiral, then the EM emission may be observable *indirectly* as it will alter the accretion rate through the magnetic torques exerted by the distorted magnetic-field lines.

All of these results indicate that the interplay of strong gravitational and EM fields represents a fertile ground for the development of interesting phenomena. Although our analysis is incomplete as the effects on plasmas are not taken into account, we believe that the main properties of the EM dynamics described above should hold as long as the energy in the black holes dominates the energy budget. A more precise estimate of the possible emissions and of the observational signatures calls for further studies which would necessarily have to include additional physics. This work, however, together with those in Refs. [7,12–15,17,18], constitute interesting first steps in this direction.

ACKNOWLEDGMENTS

[1] B. S. Sathyaprakash and B. F. Schutz, Living Rev. Relativity **12**, 2 (2009).

[2] J. S. Bloom *et al.*, arXiv:0902.1527.

[3] P. J. Armitage and P. Natarajan, Astrophys. J. Lett. **567**, L9 (2002).

[4] F. K. Liu, X.-B. Wu, and S. L. Cao, Mon. Not. R. Astron. Soc. **340**, 411 (2003).

[5] M. Milosavljevic and E. S. Phinney, Astrophys. J. **622**, L93 (2005).

[6] S. M. O'Neill, M. C. Miller, T. Bogdanovic, C. S. Reynolds, and J. Schnittman, Astrophys. J. **700**, 859 (2009).

[7] L. R. Corrales, Z. Haiman, and A. MacFadyen, arXiv:0910.0014.

[8] J. D. Schnittman and J. H. Krolik, Astrophys. J. **684**, 835 (2008).

[9] Z. Lippai, Z. Frei, and Z. Haiman, Astrophys. J. Lett. **676**, L5 (2008).

[10] G. A. Shields and E. W. Bonning, Astrophys. J. **682**, 758 (2008).

[11] M. Megevand, M. Anderson, J. Frank, E. W. Hirschmann, L. Lehner, S. L. Liebling, P. M. Motl, and D. Neilsen, Phys. Rev. D **80**, 024012 (2009).

[12] A. I. MacFadyen and M. Milosavljević, Astrophys. J. **672**, 83 (2008).

[13] P. Chang, L. E. Strubbe, K. Menou, and E. Quataert, arXiv:0906.0825.

[14] J. R. van Meter *et al.*, arXiv:0908.0023.

[15] T. Bode, R. Haas, T. Bogdanovic, P. Laguna, and D. Shoemaker, arXiv:0912.0087.

[16] R. D. Blandford and R. L. Znajek, Mon. Not. R. Astron. Soc. **179**, 433 (1977).

[17] C. Palenzuela, M. Anderson, L. Lehner, S. L. Liebling, and D. Neilsen, Phys. Rev. Lett. **103**, 081101 (2009).

[18] C. Palenzuela, L. Lehner, and S. Yoshida, arXiv:0911.3889.

[19] T. Bogdanović, C. S. Reynolds, and M. C. Miller, Astrophys. J. **661**, L147 (2007).

[20] M. Dotti, M. Volonteri, A. Perego, M. Colpi, M. Ruszkowski, and F. Haardt, Mon. Not. R. Astron. Soc.1795 (2009).

[21] C. Palenzuela, L. Lehner, O. Reula, and L. Rezzolla, arXiv:0810.1838.

[22] S. S. Komissarov, Mon. Not. R. Astron. Soc. **382**, 995 (2007).

[23] D. Pollney, C. Reisswig, E. Schnetter, N. Dorband, and P. Diener, arXiv:0910.3803.

[24] L. Baiotti, B. Giacomazzo, and L. Rezzolla, Phys. Rev. D **78**, 084033 (2008).

[25] http://www.cactuscode.org.

[26] E. Schnetter, S. H. Hawley, and I. Hawke, Classical Quantum Gravity **21**, 1465 (2004).

[27] D. Pollney, C. Reisswig, N. Dorband, E. Schnetter, and P. Diener, Phys. Rev. D **80**, 121502 (2009).

[28] L. Gunnarsen, H. Shinkai, and K. Maeda, Classical Quantum Gravity **12**, 133 (1995).

[29] A. M. Abrahams, L. Rezzolla, M. E. Rupright *et al.*, Phys. Rev. Lett. **80**, 1812 (1998).

[30] M. E. Rupright, A. M. Abrahams, and L. Rezzolla, Phys. Rev. D **58**, 044005 (1998).

[31] L. Rezzolla, A. M. Abrahams, R. A. Matzner, M. E. Rupright, and S. L. Shapiro, Phys. Rev. D **59**, 064001 (1999).

[32] A. Nagar and L. Rezzolla, Classical Quantum Gravity **22**, R167 (2005); **23**, 4297(E) (2006).

[33] L. Lehner and O. M. Moreschi, Phys. Rev. D **76**, 124040 (2007).

[34] R. M. Wald, Phys. Rev. D**10**, 1680 (1974).

[35] R. Crowley, D. Macdonald, R. Price, I. Redmount, S. K. Thorne, and X.-H. Zhang, *Black Holes: The Membrane Paradigm* (Yale University Press, New Haven, CT, 1986).

[36] M. Ansorg, B. Brügmann, and W. Tichy, Phys. Rev. D **70**,

064011 (2004).

[37] L. Rezzolla *et al.*, Astrophys. J. **679**, 1422 (2008).

[38] C. Reisswig *et al.*, Phys. Rev. D **80**, 124026 (2009).

[39] M. Koppitz, D. Pollney, C. Reisswig, L. Rezzolla, J. Thornburg, P. Diener, and E. Schnetter, Phys. Rev. Lett. **99**, 041102 (2007).

[40] D. Pollney, C. Reisswig, L. Rezzolla, B. Szilágyi, M. Ansorg, B. Deris, P. Diener, E. N. Dorband, M. Koppitz, A. Nagar *et al.*, Phys. Rev. D **76**, 124002 (2007).

[41] L. Rezzolla, E. N. Dorband, C. Reisswig, P. Diener, D. Pollney, E. Schnetter, and B. Szilágyi, Astrophys. J. **679**, 1422 (2008).

[42] L. Rezzolla, P. Diener, E. N. Dorband, D. Pollney, C. Reisswig, E. Schnetter, and J. Seiler, Astrophys. J. **674**, L29 (2008).

[43] L. Rezzolla, E. Barausse, E. N. Dorband, D. Pollney, C. Reisswig, J. Seiler, and S. Husa, Phys. Rev. D **78**, 044002 (2008).

[44] S. Husa, M. Hannam, J. A. Gonzalez, U. Sperhake, and B. Bruegmann, Phys. Rev. D **77**, 044037 (2008).

[45] M. Campanelli, C. O. Lousto, and Y. Zlochower, Phys. Rev. D **74**, 041501 (2006).

[46] M. Campanelli, C. O. Lousto, and Y. Zlochower, Phys. Rev. D **74**, 084023 (2006).

[47] M. Campanelli, C. O. Lousto, and Y. Zlochower, Phys. Rev. D **73**, 061501 (2006).

[48] A. Buonanno, L. E. Kidder, and L. Lehner, Phys. Rev. D **77**, 026004 (2008).

[49] F. Herrmann, I. Hinder, D. M. Shoemaker, P. Laguna, and R. A. Matzner, Phys. Rev. D **76**, 084032 (2007).

[50] F. Herrmann, I. Hinder, D. Shoemaker, P. Laguna, and R. A. Matzner, Astrophys. J. **661**, 430 (2007).

[51] L. Boyle, M. Kesden, and S. Nissanke, Phys. Rev. Lett. **100**, 151101 (2008).

[52] L. Boyle and M. Kesden, Phys. Rev. D **78**, 024017 (2008).

[53] P. Marronetti, W. Tichy, B. Bruegmann, J. Gonzalez, and U. Sperhake, Phys. Rev. D **77**, 064010 (2008).

[54] E. Barausse and L. Rezzolla, Astrophys. J. Lett. **704**, L40 (2009).

[55] M. Milosavljeć and E. S. Phinney, Astrophys. J. **622**, L93 (2005).

[56] N. A. Silant'ev, M. Y. Piotrovich, Y. N. Gnedin, and T. M. Natsvlishvili, arXiv:0908.2725.